Long-Range Magnetic Order in $Mn[N(CN)_2]_2(pyz)$ {pyz = pyrazine}. Susceptibility, Magnetization, Specific Heat, and Neutron Diffraction Measurements and Electronic Structure Calculations

Jamie L. Manson,*,†,‡ Qing-zhen Huang,§,⊥ Jeffrey W. Lynn,§ Hyun-Joo Koo,|| Myung-Hwan Whangbo,|| Rodney Bateman,# Takeo Otsuka,▽ Nobuo Wada,▽ Dimitri N. Argyriou,‡ and Joel S. Miller†

Contribution from the Department of Chemistry, University of Utah, Salt Lake City, Utah 84112-0850, Materials Science Division, Argonne National Laboratory, Argonne, Illinois 60439-4831, NIST Center for Neutron Research, National Institute of Standards and Technology, Gaithersburg, Maryland 20899, Department of Materials and Nuclear Engineering, University of Maryland, College Park, Maryland 20742, Department of Chemistry, North Carolina State University, Raleigh, North Carolina 27695-8204, Oxford Research Instruments, Tubney Woods, Abingdon, Oxon, U.K. OX13 5QX, and Department of Basic Science, Graduate School of Arts and Sciences, The University of Tokyo, Komaba, Meguro, Tokyo 153-8902, Japan

Received July 7, 2000

Abstract: Using dc magnetization, ac susceptibility, specific heat, and neutron diffraction, we have studied the magnetic properties of $Mn[N(CN)_2]_2(pyz)$ {pyz = pyrazine} in detail. The material crystallizes in the monoclinic space group $P2_1/n$ with $a = 7.3248(2)$, $b = 16.7369(4)$, and $c = 8.7905$ (2) Å, $\beta = 89.596$ (2)°, $V = 1077.65(7)$ Å^3, and $Z = 4$, as determined by Rietveld refinement of neutron powder diffraction data at 1.35 K. The 5 K neutron powder diffraction data reflect very little variation in the crystal structure. Interpenetrating ReO_3-like networks are formed from axially elongated Mn^{2+} octahedra and edges made up of μ-bonded $[N(CN)_2]^-$ anions and neutral pyz ligands. A three-dimensional antiferromagnetic ordering occurs below $T_N = 2.53(2)$ K. The magnetic unit cell is double the nuclear one along the *a*- and *c*-axes, giving the ($^1/_2$, 0, $^1/_2$) superstructure. The crystallographic and antiferromagnetic structures are commensurate and consist of collinear Mn^{2+} moments, each with a magnitude of 4.15(6) μ_B aligned parallel to the *a*-direction (Mn−pyz−Mn chains). Electronic structure calculations indicate that the exchange interaction is much stronger along the Mn−pyz−Mn chain axis than along the Mn−NCNCN−Mn axes by a factor of approximately 40, giving rise to a predominantly one-dimensional magnetic system. Thus, the variable-temperature magnetic susceptibility data are well described by a Heisenberg antiferromagnetic chain model, giving $g = 2.01(1)$ and $J/k_B = -0.27(1)$ K. Owing to single-ion anisotropy of the Mn^{2+} ion, field-induced phenomena ascribed to spin-flop and paramagnetic transitions are observed at 0.43 and 2.83 T, respectively.

1. Introduction

The study of molecule-based magnets is an emerging area of contemporary materials research.[1] In recent years, many examples of one-, two-, and three-dimensional (1D, 2D, and 3D) systems have been reported. Judicious choice of appropriate molecular building blocks provides the means to create a rich variety of new materials with interesting structural and magnetic properties.[2] Typically, these compounds consist of paramagnetic transition metal ions linked together by organic ligands of various sizes, shapes, and bonding motifs to afford polymeric arrays. A great deal of the modern literature describes compounds comprised of cyano,[3] oxalato,[4] or azido[5] ligands; their good superexchange properties have been attributed to favorable orbital interaction between the ligand p- and metal d-orbitals.

* To whom correspondence should be addressed. E-mail: jlmanson@anl.gov. Fax: (630) 252-9151.
† University of Utah.
‡ Argonne National Laboratory.
§ National Institute of Standards and Technology.
⊥ University of Maryland.
|| North Carolina State University.
Oxford Research Instruments.
▽ The University of Tokyo.

(1) Reviews: (a) Buchachenko, A. L. *Russ. Chem. Rev.* **1990**, *59*, 307; *Usp. Khim.* **1990**, *59*, 529. (b) Kahn, O. *Struct. Bonding* **1987**, *68*, 89. Kahn, O. *Molecular Magnetism*; VCH Publishers: New York, 1993. (c) Caneschi, A.; Gatteschi, D.; Sessoli, R.; Rey, P. *Acc. Chem. Res.* **1989**, *22*, 392. Gatteschi, D. *Adv. Mater.* **1994**, *6*, 635. (d) Miller, J. S.; Epstein, A. J.; Reiff, W. M. *Acc. Chem. Res.* **1988**, *21*, 114. (e) Miller, J. S.; Epstein, A. J.; Reiff, W. M. *Science* **1988**, *240*, 40. (f) Miller, J. S.; Epstein, A. J.; Reiff, W. M. *Chem. Rev.* **1988**, *88*, 201. (g) Miller, J. S.; Epstein, A. J. In *New Aspects of Organic Chemistry*; Yoshida, Z., Shiba, T., Ohsiro, Y., Eds.; VCH Publishers: New York, 1989. (h) Miller, J. S.; Epstein, A. J. *Angew. Chem., Int. Ed. Engl.* **1994**, *33*, 385. (i) Miller, J. S.; Epstein, A. J. *ACS Adv. Chem. Ser.* **1995**, *245*, 161.

(2) For example: (a) Pei, Y.; Verdaguer, M.; Kahn, O.; Sletten, J.; Renard, J.-P. *Inorg. Chem.* **1987**, *26*, 138. (b) Stumpf, H. O.; Ouahab, L.; Pei, Y.; Grandjean, D.; Kahn, O. *Science* **1993**, *261*, 447. (c) Borras-Almenar, J. J.; Coronado, E.; Gomez-Garcia, C. J.; Ouahab, L. *Angew. Chem., Int. Ed. Engl.* **1993**, *32*, 561. (d) Turner, S.; Kahn, O.; Rabardel, L. *J. Am. Chem. Soc.* **1996**, *118*, 6428. (e) Zhao, H.; Heintz, R. A.; Dunbar, K. R. *J. Am. Chem. Soc.* **1996**, *118*, 12844. (f) Miller, J. S.; Calabrese, J. C.; McLean, R. S.; Epstein, A. J. *Adv. Mater.* **1992**, *4*, 498. (g) Manson, J. L.; Campana, C.; Miller, J. S. *Chem. Commun.* **1998**, 251. (h) Yates, M. L.; Arif, A. M.; Manson, J. L.; Kalm, B. A.; Burkhart, B. M.; Miller, J. S. *Inorg. Chem.* **1998**, *37*, 840.

10.1021/ja0024791 CCC: $20.00
Published on Web 12/14/2000

We have employed the potentially multidentate dicyanamide ligand, $[N(CN)_2]^-$, to develop a wide range of architectures which exhibit long-range magnetic ordering. Three-coordination of $[N(CN)_2]^-$ to divalent paramagnetic metal centers affords binary rutile-like structures of $M[N(CN)_2]_2$ (M = Cr, Mn, Fe, Co, Ni, and Cu). Weak ferromagnetism was found for M = Cr, Mn, and Fe below 47,[6a] 16,[6a−c] and 19 K,[7] respectively, while the Cu analogue is only paramagnetic down to 2 K.[8] For M = Co and Ni, ferromagnetic ordering occurs below 9 and 21 K,[6d,e,7,8] respectively.

In addition to these binary systems, we have also utilized ancillary organic ligands, L, such as pyrazine (pyz),[9] 4,4′-bipyridine (4,4′-bipy),[10] and 2,2′-bipyridine (2,2′-bipy),[10] along with dicyanamide to create other lattice types. Of these $Mn[N(CN)_2]_2L$ materials, L = pyz uniquely exhibits long-range magnetic ordering above 2 K. This is directly correlated with the spatial dimensionality of their crystal structures, as the bipy-containing solids exist as isolated 1D chains while the latter forms a 3D extended network. The electron-withdrawing nature of the terminal nitrile moieties effectively diminishes the electron density on the amide-N atom, leading to reduced exchange coupling between adjacent spin carriers. Use of long spacer ligands such as $[N(CN)_2]^-$ provides the opportunity to probe low-dimensional exchange interactions and anisotropy in rigid 3D lattices. Correspondingly, Mn−NCNCN−Mn separations exceed ~7.5 Å in these materials.

Recently, the single-crystal X-ray structure and preliminary magnetic properties of $Mn[N(CN)_2]_2(pyz)$ were reported.[9] The crystal structure contains axially elongated octahedral Mn^{2+} sites which are ligated to four different μ-$[N(CN)_2]^-$ units and two axial pyrazine ligands which produce interpenetrating ReO_3-type network structures. In the present work, we describe the results of detailed magnetic, specific heat, neutron diffraction, and electronic structure studies, which unambiguously confirm 3D antiferromagnetic ordering below 2.53(2) K. Results of the temperature-dependent crystallography, including inelastic neutron scattering, will be published in due course.[11]

2. Experimental Section

Synthesis. $MnCl_2 \cdot 4H_2O$ (Baker), $Na[N(CN)_2]$ (Aldrich), pyrazine, and pyrazine-d_4 (Aldrich) were used as purchased. Doubly deionized water was used in all sample preparations. To a vigorously stirring aqueous solution containing both $Na[N(CN)_2]$ (0.072 mol, 6.4029 g) and pyrazine-d_4 (0.036 mol, 3.0249 g) was added an aqueous solution of $MnCl_2 \cdot 4H_2O$ (0.036 mol, 7.1166 g). A pale yellow precipitate formed immediately, which was stirred for an additional 4 h to ensure complete reaction. The solid was collected via vacuum filtration, washed with copius amounts of fresh water, and dried in vacuo over P_2O_5 for 8 h, yielding 7.1601 g (74%) of the desired product. Sample quality was judged by both infrared spectroscopy and X-ray powder diffraction. Nondeuterated $Mn[N(CN)_2]_2(pyz)$ was synthesized as described previously.[9]

Magnetic Measurements. Direct current (dc) magnetization measurements were carried out between 2 and 300 K utilizing a Quantum Design MPMS-5XL SQUID ac/dc magnetometer equipped with a reciprocating sample operation transport, enhanced low-temperature thermometry, ultralow field, and magnet reset options. To perform low-field M(T) experiments, the μ-metal shield was degaussed, the magnet was reset, and a Hall probe was utilized to null any residual magnetic field prior to sample insertion. Alternating current (ac) susceptibility measurements were performed between 2 and 10 K using a 1 Oe ac drive field oscillating at 10, 100, and 1000 Hz. Ultralow-temperature $\chi_{ac}(T)$ magnetic susceptibilities were recorded on a home-built measurement system based on a Conductus, Inc. SQUID magnetometer equipped with a home-made dilution refrigerator. An oscillating field of 175 Hz at an amplitude of a few millioersted (mOe) was used. The geomagnetic field was shielded by μ-metal, so that the static field at the sample was less than 10 mOe. Values of the molar ac susceptibilities were calculated, so that they were smoothly connected to the extrapolation of the high-temperature data. Field-dependent ac susceptibility measurements were performed using a 1 Oe ac amplitude oscillating at 10 Hz in an applied dc magnetic field up to 5 T. Zero-field-cooled dc magnetization studies were performed at 0.1, 1, 10, and 50 Oe, and data were taken upon warming. Field-cooled dc magnetization data were obtained by cooling in an applied field from 10 K down to 2 K, and data were collected upon warming. Powdered samples weighing approximately 15−20 mg were loaded in gelatin capsules and mounted in a plastic straw. High-field $M(H)$ experiments up to 12 T were conducted on an Oxford Research Instruments 12 T MAG-LAB vibrating sample magnetometer (VSM). All magnetic data were corrected for core diamagnetism using a standard value of -110×10^{-6} emu/mol as obtained from Pascal's constants.

Specific Heat. Temperature- and field-dependent specific heat, C_p, measurements were carried out using an Oxford Research Instruments Heliox system equipped with a superconducting 12/14 T dc magnet and ^{3}He insert. The system utilizes a relaxation technique and consists of a sapphire chip suspended on eight gold-plated tungsten wires. A pelletized sample weighing 1.4 mg was attached to the chip using approximately 200 μg of Wakefield thermal compound. The chip has an integral Cernox thermometer and a sputtered gold alloy heater. Temperature stability was determined to be within 0.002 K at all chip temperatures. Specific heat was measured in dc fields of 0 and 0.43 T between 1 and 3.5 K at intervals of 0.03 K, which required 57 h to complete. Three pairs of transients (three up and three down) per data point were acquired at each temperature interval with a maximum height of 0.06 K. Prior to field-dependent studies, the chip temperature was reset to 2 K. For $C_p(H)$ measurements, one pair of transients per data point with a height of 3% (or 0.06 K) was utilized. A magnetic field sweep of 100 Oe/min was selected while a decreased field sweep of

(3) (a) Ferlay, S.; Mallah, T.; Ouahes, R.; Veillet, P.; Verdaguer, M. *Nature* **1995**, *378*, 701. (b) Larionova, J.; Sanchiz, J.; Gohlen, S.; Ouahab, L.; Kahn, O. *Chem. Commun*. **1998**, 953. (c) Gadet, V.; Mallah, T.; Castro, I.; Verdaguer, M. *J. Am. Chem. Soc.* **1992**, *114*, 9213. (d) Mallah, T.; Ferlay, S.; Auberger, C.; Helary, C.; L'Hermite, F.; Ouahes, F.; Vaissermann, J.; Verdaguer, M.; Veillet, P. *Mol. Cryst., Liq. Cryst.* **1995**, *273*, 141. (e) Entley, W. R.; Girolami, G. S. *Science* **1995**, *268*, 397. (f) Holmes, S. M.; Girolami, G. S. *J. Am. Chem. Soc*. **1999**, *121*, 5593. (g) Hatlevik, O.; Buschmann, W. E.; Zhang, J.; Manson, J. L.; Miller, J. S. *Adv. Mater*. **1999**, *11*, 914.

(4) For example: (a) Tamaki, H.; Zhong, Z. J.; Matsumoto, N.; Kida, S.; Koikawa, K.; Achiwa, N.; Okawa, H. *J. Am. Chem. Soc*. **1992**, *114*, 6974. (b) Mathoniere, C.; Nuttall, C. J.; Carling, S. G.; Day, P. *Inorg. Chem.* **1996**, *35*, 1201. (c) Decurtins, S.; Schmalle, H. W.; Schneuwly, P.; Ensling, J.; Gütlich, P. *J. Am. Chem. Soc*. **1994**, *116*, 9521.

(5) (a) Manson, J. L.; Arif, A. M.; Miller, J. S. *Chem. Commun*. **1999**, 1479. (b) Shen, H.-Y.; Bu, W.-M.; Gao, E.-Q.; Liao, D.-Z.; Jiang, Z.-H.; Yan, S.-P.; Wang, G.-L. *Inorg. Chem*. **2000**, *39*, 396. (c) Mautner, F. A.; Cortés, R.; Lezama, L.; Rojo, T. *Angew. Chem., Int. Ed. Engl*. **1996**, *35*, 78. (d) Gregson, A. K.; Moxon, N. T. *Inorg. Chem*. **1982**, *21*, 586. (e) Escuer, A.; Vicente, R.; Goher, M. A. S.; Mautner, F. A. *Inorg. Chem*. **1996**, *35*, 6386. (f) Escuer, A.; Vicente, R.; Goher, M. A. S.; Mautner, F. A. *Inorg. Chem*. **1998**, *37*, 782. (g) Thompson, L. K.; Tandon, S. S.; Lloret, F.; Cano, J.; Julve, M. *Inorg. Chem*. **1997**, *36*, 3301. (h) Cortés, R.; Lezama, L.; Pizarro, J. L.; Arriortua, M. I.; Rojo, T. *Angew. Chem., Int. Ed. Engl*. **1996**, *35*, 1810. (i) Han, S.; Manson, J. L.; Kim, J. K.; Miller, J. S. *Inorg. Chem*. **2000**, *39*, 4182.

(6) (a) Manson, J. L.; Kmety, C. R.; Epstein, A. J.; Miller, J. S. *Inorg. Chem*. **1999**, *38*, 2552. (b) Kmety, C. R.; Huang, Q.-z.; Lynn, J. W.; Erwin, R. W.; Manson, J. L.; McCall, S.; Crow, J. E.; Stevenson, K. L.; Miller, J. S.; Epstein, A. J. *Phys. Rev. B* **2000**, *62*, 5576. (c) Batten, S. R.; Jensen, P.; Kepert, C. J.; Kurmoo, M.; Moubaraki, B.; Murray, K. S.; Price, D. J. *J. Chem. Soc., Dalton Trans*. **1999**, 2987. (d) Manson, J. L.; Kmety, C. R.; Huang, Q.-z.; Lynn, J. W.; Bendele, G.; Pagola, S.; Stephens, P. W.; Epstein, A. J.; Miller, J. S. *Chem. Mater*. **1998**, *10*, 2552. (e) Batten, S. R.; Jensen, P.; Moubaraki, B.; Murray, K. S.; Robson, R. *Chem. Commun*. **1998**, 439.

(7) Kurmoo, M.; Kepert, C. J. *New J. Chem*. **1998**, 1515.

(8) Kurmoo, M.; Kepert, C. J. *Mol. Cryst. Liq. Cryst*. **1999**, *334*, 693.

(9) Manson, J. L.; Incarvito, C. D.; Rheingold, A. L.; Miller, J. S. *J. Chem. Soc., Dalton Trans*. **1998**, 3705.

(10) Manson, J. L.; Incarvito, C. D.; Arif, A. M.; Rheingold, A. L.; Miller, J. S. *Mol. Cryst. Liq. Cryst*. **1999**, *334*, 605.

(11) Brown, C. M.; Manson, J. L.; Huang, Q.-z.; Lynn, J. W., manuscript in preparation.

Table 1. Exponents ζ_i and Valence Shell Ionization Potentials H_{ii} of Slater-Type Orbitals χ_i Used for Extended Hückel Tight-Binding Calculation[a]

atom	χ_i	H_{ii} (eV)	ζ_i	c_1[b]	ζ_i'	c_2[b]
Mn	4s	−9.75	1.844	1.0		
Mn	4p	−5.89	1.350	1.0		
Mn	3d	−11.7	5.767	0.3898	2.510	0.7297
C	2s	−21.4	1.831	0.7616	1.153	0.2630
C	2p	−11.4	2.730	0.2595	1.257	0.8026
N	2s	−26.0	2.261	0.6978	1.425	0.3304
N	2p	−13.4	3.249	0.2881	1.499	0.7783
H	1s	−13.6	1.300	1.0		

[a] H_{ii}'s are the diagonal matrix elements $\langle\chi_i|H^{\text{eff}}|\chi_i\rangle$, where H^{eff} is the effective Hamiltonian. In our calculations of the off-diagonal matrix elements, $H^{\text{eff}} = \langle\chi_i|H^{\text{eff}}|\chi_j\rangle$, the weighted formula was used. See: Ammeter, J.; Bürgi, H.-B.; Thibeault, J.; Hoffmann, R. *J. Am. Chem. Soc*. **1978**, *100*, 3686. [b] Contraction coefficients used in the double-ζ Slater-type orbital.

10 Oe/min was used in the regions above and below the phase transition. The specific heat was measured continuously taking 800 s/point (0.13 T intervals) below the transition and decreasing to 260 s/point (0.043 T intervals) above it.

Crystal and Magnetic Structure Studies. Neutron powder diffraction measurements on $Mn[N(CN)_2]_2(pyz\text{-}d_4)$ were made using all 32 detectors of the BT-1 high-resolution powder diffractometer at the NIST Center for Neutron Research using a neutron wavelength of 1.5401 Å produced by a copper (311) monochromator. Collimators with horizontal divergences of 15, 20, and 7′ in arc were used for the in-pile, monochromatic, and diffracted beams, respectively. Intensities were measured in steps of 0.05° in the 2θ range of 3−165° at 1.35 and 5 K. A powder sample weighing ∼6.0 g was loaded into a vanadium can, mounted in an ILL-type top loading orange cryostat, and positioned in the center of the neutron beam. Crystal and magnetic structure refinements were carried out using the GSAS[12] program. The neutron scattering amplitudes used in refinements are −0.373, 0.930, 0.665, and 0.667 for Mn, N, C, and D, respectively.[12] The initial structural model and atomic coordinates used in the refinement were those derived from the single-crystal X-ray analysis.[9]

To aid with the magnetic structure determination, detailed measurements were performed with the high-intensity BT-9 triple-axis spectrometer using a neutron wavelength of 2.359 Å defined by a pyrolytic graphite (PG) monochromator. A PG filter was placed in front of the monochromator to suppress any higher-order wavelength contaminations. Intensity patterns were collected in the range $10° \le 2\theta \le 45°$ at 1.35 and 5 K. Difference patterns clearly indicated the presence of magnetic Bragg reflections at the lower temperature. The magnetic order parameter was recorded by measuring the intensity of the strong (111) magnetic Bragg peak as a function of both increasing and decreasing temperature, which exhibited negligible hysteresis.

Spin Dimer Analysis. Spin exchange interactions in $Mn[N(CN)_2]_2$(pyz) were examined in terms of the spin−orbital interaction energies Δe calculated for its spin dimers using the extended Hückel molecular orbital method.[13] Our calculations were carried out by employing the CAESAR program package,[14] and the atomic orbital parameters of Mn, C, N, and O are listed in Table 1. In our calculations for the Δe values, double-ζ Slater-type orbitals[15] were used for the 3d-orbitals of Mn and 2s/2p-orbitals of C and N, because such orbitals have been found to reproduce the trends in the spin exchange parameters of numerous magnetic solids.[16−19]

3. Results and Discussion

3.1. Magnetic Properties: Temperature Dependence. The variable-temperature magnetic susceptibility, $\chi_{dc}(T)$, of a polycrystalline sample of $Mn[N(CN)_2]_2$(pyz) was measured between 2 and 300 K and fit to the Curie−Weiss expression, $\chi \propto (T - \theta)^{-1}$, giving $g = 2.01(1)$ and $\theta = -4.06(6)$ K, which indicates weak antiferromagnetic coupling between the Mn^{2+} sites. At 300 K, the $\chi_{dc}T(T)$ value is 4.370 emu·K/mol, in excellent agreement with the expected value (4.375 emu·K/mol) for isolated $S = {}^5/_2$ Mn^{2+} ions. Due to antiferromagnetic coupling, $\chi_{dc}T(T)$ decreases rapidly below approximately 50 K, reaching a value of 1.04 emu·K/mol at 2 K. The 1D linear chain compound $Mn[N(CN)_2]_2(py)_2$ (py = pyridine) also contains Mn−N≡C−N−C≡N−Mn bridges, and a weak antiferromagnetic coupling was observed ($\theta = -1.8$ K, $J/k_B = -0.10$ K), suggesting enhanced spin coupling via the pyrazine bridges.[20] The spin dimer analysis for $Mn[N(CN)_2]_2$(pyz) (see section 3.4) reveals that the spin exchange interactions through the pyrazine units are much stronger than those through the $[N(CN)_2]^-$ bridges. Hence, to a first approximation, the magnetic susceptibility data can be described very well by the Heisenberg 1D antiferromagnetic chain model ($H = -JS_1 \cdot S_2$) developed by Fisher for classical $S = {}^5/_2$ spins (eq 1),[21]

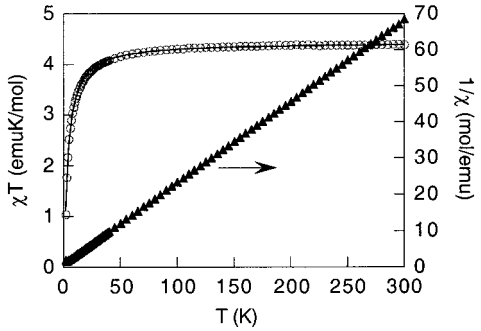

Figure 1. Temperature dependence of the $\chi_{dc}T$ (○) product and the reciprocal molar magnetic susceptibility, $1/\chi_{dc}$ (▲), of $Mn[N(CN)_2]_2$(pyz) between 2 and 300 K. The full line represents the theoretical fit to eq 1 with $g = 2.01(1)$, $J/k_B = -0.27(1)$ K.

$$\chi_{1D} = \frac{Ng^2\mu_B{}^2S(S+1)}{3k_BT}\frac{1+u(K)}{1-u(K)} \qquad (1)$$

where $u(K) = \coth\{2JS(S+1)/k_BT\} - \{k_BT/2JS(S+1)\}$ and N, g, μ_B, and k_B have their usual meanings. The best fit obtained using eq 1 yielded $g = 2.01(1)$ and $J/k_B = -0.27(1)$ K (Figure 1). An identical spin exchange parameter is obtained from

$$k_BT_{max}/J = 1.12S(S+1) + 0.10 \qquad (2)$$

which relates the J value of a 1D magnetic system to the temperature, T_{max}, at which point $\chi(T)$ reaches a maximum.[22] This lends further support that $Mn[N(CN)_2]_2$(pyz) is a quasi-1D magnetic system.

With the large metal−metal separations imparted by the $[N(CN)_2]^-$ bridging unit (8.719 Å average), exchange along Mn−NCNCN−Mn should be significantly reduced. It is evident

(12) Larson, A. C.; Von Dreele, R. B. *GSAS: General Structure Analysis System*; Los Alamos National Laboratory Report No. LAUR-86-748; Los Alamos National Laboratory: Los Alamos, NM, 1990.
(13) Hoffmann, R. *J. Chem. Phys*. **1967**, *39*, 1397.
(14) Ren, J.; Liang, W.; Whangbo, M.-H. *Crystal and Electronic Structure Analysis Using CAESAR*; 1998. This book can be downloaded from the web site http://www.PrimeC.com/.
(15) Clementi, E.; Roetti, C. *Atomic Data Nuclear Data Tables* **1974**, *14*, 177.
(16) Lee, K. S.; Koo, H.-J.; Whangbo, M.-H. *Inorg. Chem*. **1999**, *38*, 2199.
(17) Koo, H.-J.; Whangbo, M.-H. *Solid State Commun*. **1999**, *111*, 353.
(18) Whangbo, M.-H.; Koo, H.-J.; Lee, K.-S. *Solid State Commun*. **2000**, *114*, 27.
(19) Koo, H.-J.; Whangbo, M.-H. *J. Solid State Chem*. **2000**, *151*, 96.
(20) (a) Manson, J. L.; Arif, A. M.; Incarvito, C. D.; Liable-Sands, L. M.; Rheingold, A. L.; Miller, J. S. *J. Solid State Chem*. **1999**, *145*, 369. (b) The reported J value was obtained by the Hamiltonian $-JS_1 \cdot S_2$.
(21) Fisher, M. E. *Am. J. Phys*. **1964**, *32*, 343.
(22) Lines, M. E. *J. Phys. Chem. Solids* **1970**, *31*, 101.

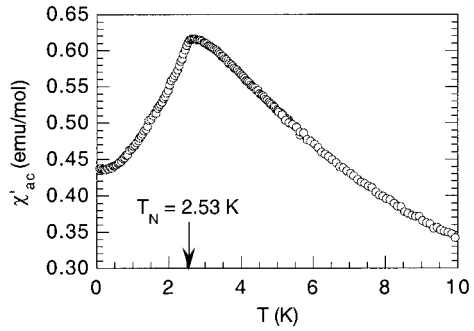

Figure 2. $\chi'_{ac}(T)$ data displaying the cusp associated with the magnetic phase transition.

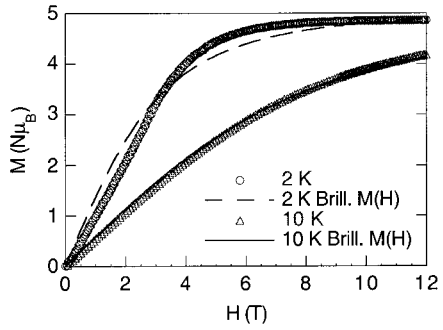

Figure 3. Isothermal magnetization data for $Mn[N(CN)_2]_2(pyz)$ acquired at 2 and 10 K. The dashed and full lines represent the best fit of the data to the Brillioun magnetization.

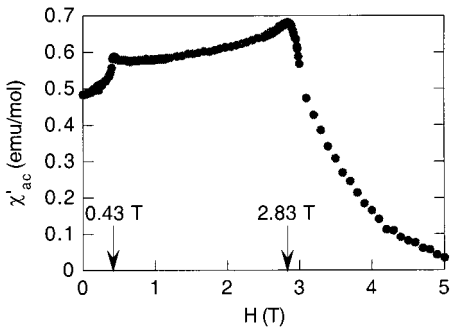

Figure 4. $\chi'_{ac}(H)$ obtained at 2 K.

that the powder susceptibility is only sensitive to a single parameter, as fits to other theoretical models (2D and 3D) give essentially identical J/k_B values. Single-crystal susceptibility measurements are needed to assess the magnitude and sign of the individual exchange interactions (see section 3.4).

Evidence for long-range 3D antiferromagnetic ordering is demonstrated by a sharp cusp in $M(T)$ and $\chi(T)$ at 2.7 K (Figure 2). A maximum in $\chi(T)$ arises as a result of short-range ordering while the actual 3D magnetic ordering temperature, $T_N \approx 2.5$ K, lies just below the maximum and may be determined from a plot of $d\chi T(T)/dT$.[21] The ratio of T_N/θ gives a value of 0.62, which is less than the value expected for a simple cubic ($z = 6$) Heisenberg lattice (0.72).[23] By comparison, perovskite-like $RbMnF_3$ affords $T_N/\theta = 0.70$.[24] The in-phase component of the ac susceptibility, $\chi'(T)$, was measured down to 70 mK and is frequency independent, which precludes glassy-like behavior associated with a spin-disordered ground state,[25] while the out-of-phase component, $\chi''(T)$, is zero, as expected for a collinear antiferromagnet below T_N. The extrapolated value of the ac susceptibility at 0 K was found to be 0.43 emu/mol and is in good agreement with the expected value of $2\chi_{max}(T)/3$, which further supports 3D magnetic ordering in the material. Zero-field-cooled and field-cooled magnetization, $M(T)$, carried out in small applied magnetic fields ($H \leq 50$ Oe), failed to demonstrate irreversibility attributable to spin canting, in contrast to that observed for the noncollinear antiferromagnet $Mn[N(CN)_2]_2$.[6a−c]

Field Dependence. Isothermal magnetization measurements performed at 2 and 10 K to 12 T demonstrate behavior typical of an antiferromagnet in the ordered and paramagnetic regimes, respectively (Figure 3). The magnetization rises nearly linearly to about 3.40 N·μ_B (at 3 T) and then increases more slowly, reaching a saturation value of 4.87 N·μ_B at 10 T. This value is in excellent agreement with the value computed for the Brillioun magnetization for $S = {}^5/_2$ Mn^{2+} ions. In the antiferromagnetically ordered state, the measured magnetization is expected to rise more slowly than the Brillouin magnetization. Fitting of the 10 K $M(H)$ data to the Brillioun function yields a very good agreement, giving the same g and θ values as those obtained from the Curie−Weiss fit. Conveniently, the relatively low saturation field is a result of the small J/k_B value, which allows us to determine exchange and anisotropy parameters as described below.

Weak Anisotropy and Spin-Flop Behavior. At temperatures below T_N, the magnetization of a typical antiferromagnet is expected to initially increase with constant slope upon increasing H, and then saturating asymptotically at the saturation magnetization, M_s. On occasion, some antiferromagnets possess a small degree of single-ion or exchange anisotropy, which gives rise to a specific field dependence known as a spin-flop transition at some critical field, H_{sf}.[26] At H_{sf}, the spins favor a preferred alignment relative to the easy axis of magnetization (i.e., a crystallographic axis along which spins of an antiferromagnetic system align). If H is applied parallel to the easy axis, the moments will tend to reorient themselves perpendicular to H, giving rise to a first-order phase transition. This transition is manifested as a discontinuity in $M(H)$ upon crossing the AF−SF phase boundary. Alternatively, this may be obtained directly by measuring the differential susceptibility as a function of H, $\chi'(H)$, resulting in a broad (powders) or sharp peak (single crystals). Upon further increasing H, the sublattice moments gradually rotate until another critical field, H_c, is reached, beyond which the average spin direction is parallel to the easy axis. This is a second-order transition to a paramagnetic phase, for which $M(H)$ is continuous but $\chi'(H)$ is discontinuous. Between the transition fields, $M(H)$ increases linearly with H. The critical fields H_{sf} and H_c may be quantitatively defined as eqs 3 and 4, where H_E and H_A represent the exchange and anisotropy fields, respectively. As expected, these critical fields are highly dependent upon temperature.

$$H_{sf} = \sqrt{2H_E H_A - H_A^2} \tag{3}$$

$$H_c = 2H_E - H_A \tag{4}$$

For $Mn[N(CN)_2]_2(pyz)$, H_{sf} and H_c were experimentally found to be 0.43 and 2.83 T, respectively, by measuring $\chi'(H)$ (Figure 4). From eqs 3 and 4, $H_A = 0.065$ T and $H_E = 1.45$ T at 2 K. A similar H_A value (i.e., 0.063 T) has been reported for the 2D layered compound $(C_3H_7NH_3)_2MnBr_4$.[27] The H_A/H_E ratio of 4.5 $\times 10^{-2}$ is of the same order of magnitude as that observed for

(23) de Jongh, L. J.; Miedema, A. R. *Adv. Phys.* **1974**, *23*, 1.
(24) Teaney, D. T.; Moruzzi, V. L.; Argyle, B. E. *J. Appl. Phys.* **1966**, *37*, 1122.
(25) Mydosh, J. A. *Spin Glasses: An Experimental Introduction*; Taylor and Francis: London, 1993.
(26) Carlin, R. L.; van Duyneveldt, A. J. *Acc. Chem. Res.* **1980**, *13*, 231.

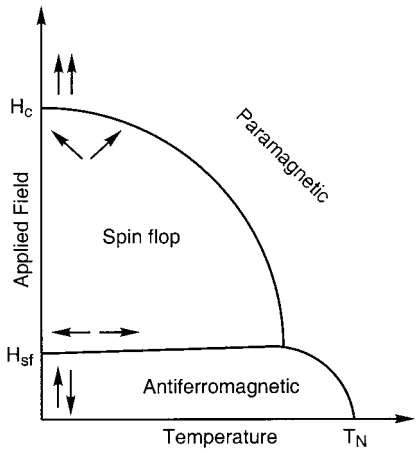

Figure 5. Schematic representation of the H/T phase diagram for a weakly anisotropic antiferromagnet. Note the regions of the spin-flop and paramagnetic phases.

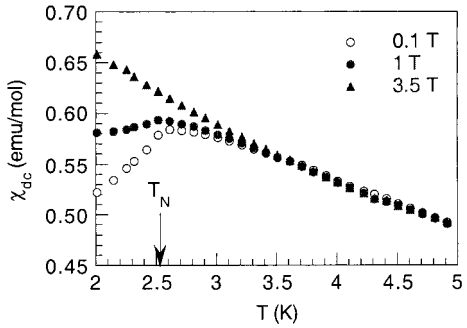

Figure 6. $\chi_{dc}(T)$ data taken at various external fields in the vicinity of T_N.

MnF_2 (1.6×10^{-2})[28] but somewhat larger than that calculated for $Mn[N(CN)_2]_2$ (1×10^{-3}).[6b] The Lande g value of 2.01 obtained for $Mn[N(CN)_2]_2(pyz)$ reflects some degree of anisotropy, likely imposed by the tetragonal distortion of the Mn^{2+} ion. Equations 3 and 4 show that an increase in H_A increases H_{sf} but reduces H_c. When $H_E = H_A$, the anisotropy is so large that the spin-flop phase is no longer energetically favorable and the moments undergo a metamagnetic transition from the antiferromagnetic ground state to a ferromagnetic excited state. Figure 5 presents a schematic illustration of a magnetic phase diagram for a weakly anisotropic antiferromagnet. At a specific temperature just below T_N, H_{sf} and H_c intersect at the tricritical point, which indicates the coexistence of the antiferromagnetic, spin-flop, and paramagnetic phases.

To further substantiate evidence for the spin-flop transition, additional $\chi_{dc}(T)$ measurements at several dc fields were carried out (Figure 6). The data for $H < H_{sf}$ clearly show the antiferromagnetic transition near 2.5 K, i.e., a pronounced decrease in the susceptibility below T_{max}. When $H_{sf} < H < H_c$, we obtain χ_{perp}, as expected. Increasing the field beyond H_c induces a paramagnetic state.

Owing to the structural distortion of the MnN_6 octahedra, single-ion anisotropy likely plays a role in the overall magnetic properties. For a Mn^{2+} ion in an octahedral crystal field, the orbital ground state is $^6A_{1g}$, which is split into three Kramers doublets by second-order spin−orbit coupling. At low temperature, all three doublets are thermally populated, leading to an effective $S = {}^5/_2$ system. Furthermore, the axial distortion often leads to a zero-field splitting at low temperatures, and $D/k_B < 0$ since the distortion is an axial elongation (see section 3.3). From the H_{sf}, H_A, and H_E values, D/k_B is estimated to be −0.022 K. This value, an order of magnitude smaller than J/k_B, is reasonable for Mn^{2+} ions.[27]

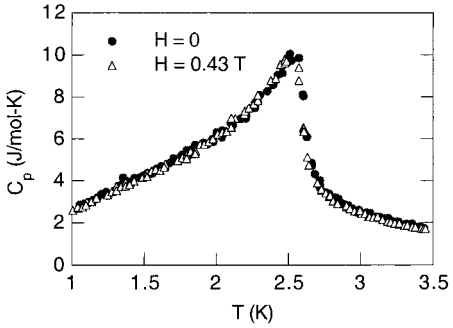

Figure 7. Specific heat as a function of temperature, $C_p(T)$, of $Mn[N(CN)_2]_2(pyz)$ taken in external dc fields of 0 and 0.43 T.

3.2. Specific Heat: Temperature-Dependent Studies. The specific heat as a function of temperature, $C_p(T)$, for $Mn[N(CN)_2]_2(pyz)$ was measured in applied magnetic fields of $H = 0$ and $H = 0.43$ T (Figure 7). A λ-shaped anomaly is observed at ~2.5 K, which indicates 3D long-range magnetic ordering and is consistent with the magnetic susceptibility measurements. In this temperature regime, the lattice and electronic contributions to the specific heat are negligible, and the origin of the anomaly is largely magnetic. The gradual rise of $C_p(T)$ just above T_N is due to increasing short-range magnetic correlations. In an applied field of 0.43 T, i.e., H_{sf}, the peak width and height remain unchanged, owing to an equilibrium between the spin states aligned parallel to and perpendicular to the magnetic field. The change in magnetic entropy, ΔS_M, can be obtained by integrating the $C_p(T)$ versus T curve between 0.9 and 3.4 K, which gives a value of 5.9 J/mol·K.[29] Extrapolation of the $C_p(T)$ data below 0.9 K to $T = 0$ gives an additional 1.2 J/mol·K to ΔS_M. Typically, the total magnetic entropy for N spins with a spin value of S approaches the value of $Nk_B \ln(2S + 1)$. In the present case, $S = {}^5/_2$ and ΔS_M should approach $Nk_B \ln(6) = 14.9$ J/mol·K. The total magnetic entropy change of $Mn[N(CN)_2]_2(pyz)$ is estimated to be 7.1 J/mol·K, which corresponds to 48% of $Nk_B \ln(6)$. We are unable to estimate J/k_B from the $C_p(T)$ data because a Heisenberg model for $S = {}^5/_2$ is not available.

Field-Dependent Studies. To confirm and identify the type of field-induced magnetic phase transitions found in the other studies, we performed isothermal specific heat measurements at 2 K (Figure 8). The $C_p(H)$ data yielded a single anomaly at 2.83 T, which is attributed to the spin-flop to paramagnetic phase transition as suggested by the $M(H)$ data. Although the spin-flop transition is first-order, it is difficult to detect using this technique.

3.3. Neutron Diffraction: Low-Temperature Crystal Structure. Owing to the large incoherent scattering cross section of hydrogen,[30] it was necessary to synthesize a deuterated sample of $Mn[N(CN)_2]_2(pyz)$. Neutron powder diffraction patterns were obtained on BT-1 at 1.35 and 5 K and are shown in Figures 9 and 10, respectively. The nuclear structure was refined in the monoclinic space group $P2_1/n$ at each temperature using Rietveld

(27) Groenendijk, H. A.; van Duyneveldt, A. J.; Willett, R. D. *Physica* **1979**, *98B*, 53.

(28) (a) Keffer, F. *Phys. Rev. B* **1952**, *87*, 608. (b) Jacobs, I. S. *J. Appl. Phys*. **1961**, *32*, 61S. (c) Trapp, C.; Stout, J. W. *Phys. Rev. Lett*. **1963**, *10*, 157.

(29) Kittel, C. *Introduction to Solid State Physics*; Wiley and Sons: New York, 1986.

(30) Bacon, G. E. *Neutron Diffraction*; Clarendon Press: Oxford, 1975.

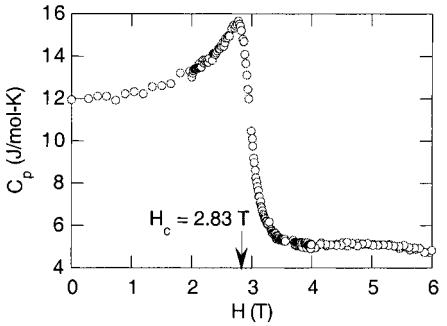

Figure 8. Field-dependent specific heat, $C_p(H)$, obtained at 2 K.

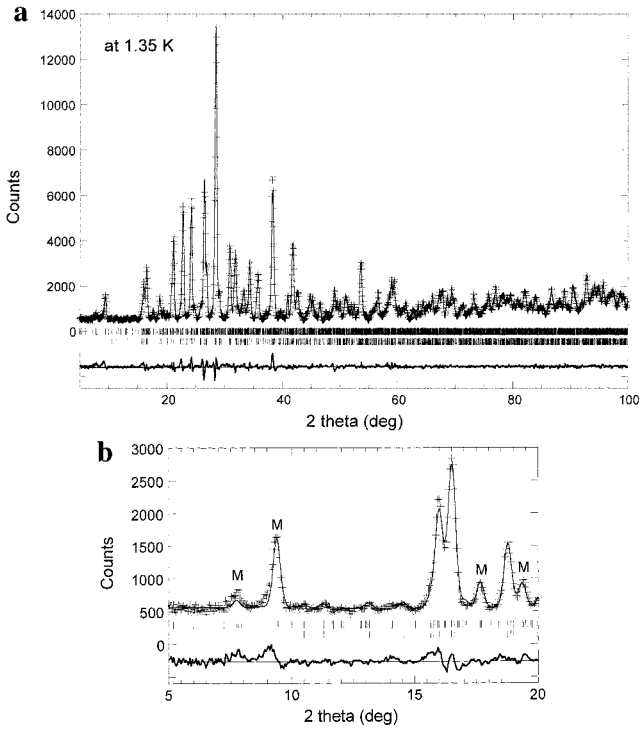

Figure 9. Neutron diffraction data for Mn[N(CN)$_2$]$_2$(pyz) taken at 1.35 K. (a) Full neutron diffraction pattern ($3 \le 2\theta \le 165°$) showing the observed (+), calculated (−), and the difference between I_{obs} and I_{calc} is shown as a heavy line at the bottom. (b) Low-angle data emphasizing the Rietveld refinement of the magnetic Bragg peaks (M). Upper and lower tics correspond to magnetic and nuclear reflections, respectively.

analysis. Selected interatomic distances and angles are provided in Table 2. The lattice parameters were determined to be a = 7.3248(2), b = 16.7369(4), and c = 8.7905(2) Å, β = 89.596(2)°, and V = 1077.65(7) Å^3 [R_p = 2.91%, R_{wp} = 3.47%, and χ^2 = 2.495] at 1.35 K and a = 7.3252(1), b = 16.7372(1), and c = 8.7908(2) Å, β = 89.597(2)°, and V = 1077.76(4) Å^3 [R_p = 2.96%, R_{wp} = 3.40%, and χ^2 = 1.832] at 5 K, i.e., below and above T_N, respectively. Each nuclear unit cell contains four asymmetric units, and none of the atoms reside on special positions. Importantly, a structural phase transition does not accompany the magnetic phase transition, and the unit cell volume increases only slightly upon warming.

Since there is little structural variation between 1.35 and 5 K, our discussion will focus on the results obtained at the lower temperature. The coordination geometry of the Mn^{2+} center is axially elongated with four equatorial $[N(CN)_2]^-$ ligands and two axial pyz molecules (Figure 11). The dicyanamide ligands are not coordinated symmetrically, with Mn−N$_{eq}$ bond distances ranging from 2.14(1) to 2.24(1) Å. The Mn−N$_{ax}$ bond distances of 2.27(1) and 2.29(1) Å are, however, equivalent and longer

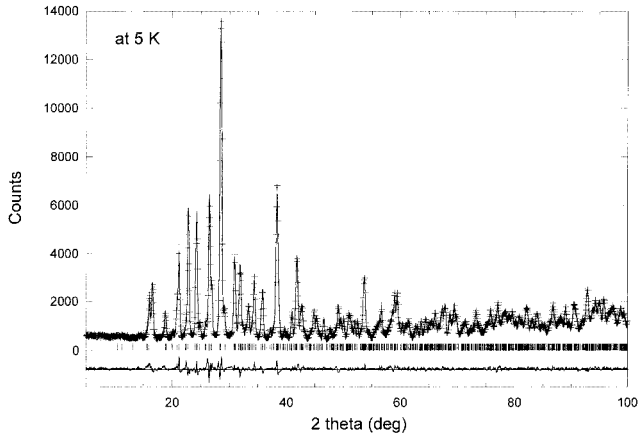

Figure 10. Observed (+), calculated (−), and difference neutron powder diffraction pattern for Mn[N(CN)$_2$]$_2$(pyz) at 5 K. Tics indicate reflection positions for the nuclear phase.

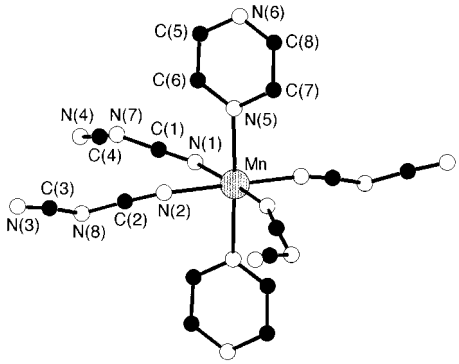

Figure 11. Molecular structure and atom labeling scheme showing only the Mn^{2+} coordination environment as found in Mn[N(CN)$_2$]$_2$(pyz). Deuterium atoms have been omitted for clarity.

than Mn−N$_{eq}$ due to the steric bulk of the pyz molecule. Other than the structural elongation of the Mn^{2+} ion, the N−Mn−N′ bond angles reflect a small deformation from the ideal 90 and 180° geometries, the largest discrepancies being 82.9(3) and 174.8(5)°. The $[N(CN)_2]^-$ ligand adopts a pseudo-C_{2v} symmetry, with terminal C−N and amide N−C distances ranging from 1.155(6) to 1.191(6) and from 1.282(7) to 1.327(6) Å, which indicate triple- and single-bond character, respectively, as typically observed for this bonding mode.[20]

The extended structure of Mn[N(CN)$_2$]$_2$(pyz) consists of polymeric 3D networks similar to ReO_3 (Figure 12). Nominal square-like grids comprised of Mn−NCNCN−Mn edges reside in the *bc*-plane, while pyz ligands link them together to afford 1D Mn−pyz−Mn chains along the *a*-axis. In terms of the lattice parameters, the intramolecular Mn···Mn separations are given by *a*, 0.517*b*, and *c*. Due to the formation of large pores, solvent molecules do not intercalate, but interpenetration of a second lattice occurs, which leads to a considerably shorter intermolecular Mn···Mn distance of 6.42 Å.

Zero-Field Magnetic Structure. At 1.35 K, no fewer than four additional reflections are observed (Figure 9),which are ascribed to long-range magnetic ordering in the material, as verified by higher intensity BT-9 data. As the dicyanamide and pyrazine ligands are diamagnetic, the magnetic diffraction pattern originates solely from spin ordering of the Mn^{2+} ions. The magnetic unit cell is double the nuclear cell along the *a* and *c* crystallographic axes, yielding the ($^1/_2$, 0, $^1/_2$) superstructure. It contains 16 Mn ions, since there are only four in each nuclear unit cell. The superlattice reflections show the occurrence of 3D antiferromagnetic ordering.

Table 2. Selected Interatomic Distances (Å) and Angles (Deg) for $Mn[N(CN)_2]_2(pyz)$ As Determined from Neutron Powder Diffraction at 1.35 and 5 K

	1.35 K	5 K
Mn−N(1)	2.240(9)	2.24(1)
Mn−N(2)	2.22(1)	2.23(1)
Mn−N(3)	2.15(1)	2.14(1)
Mn−N(4)	2.194(9)	2.20(1)
Mn−N(5)	2.27(1)	2.27(1)
Mn−N(6)	2.29(1)	2.26(1)
C(1)−N(1)	1.191(6)	1.185(6)
C(1)−N(7)	1.282(7)	1.297(7)
C(4)−N(7)	1.300(6)	1.294(6)
C(4)−N(4)	1.164(6)	1.165(6)
C(2)−N(2)	1.158(6)	1.160(6)
C(2)−N(8)	1.296(6)	1.290(6)
C(3)−N(8)	1.327(6)	1.324(6)
C(3)−N(3)	1.155(6)	1.161(3)
N(1)−Mn−N(2)	82.9(3)	83.1(3)
N(1)−Mn−N(3)	93.7(3)	94.1(4)
N(1)−Mn−N(4)	175.0(5)	174.8(5)
N(1)−Mn−N(5)	88.8(3)	88.6(4)
N(1)−Mn−N(6)	90.1(4)	90.2(4)
N(2)−Mn−N(3)	176.3(5)	177.2(5)
N(2)−Mn−N(4)	92.0(3)	91.7(4)
N(2)−Mn−N(5)	88.5(4)	89.1(4)
N(2)−Mn−N(6)	89.5(4)	89.8(4)
N(5)−Mn−N(6)	178.3(5)	178.0(5)
Mn−N(1)−C(1)	144.2(4)	144.1(4)
Mn−N(2)−C(2)	154.4(4)	153.8(4)
Mn−N(3)−C(3)	165.7(5)	164.7(5)
Mn−N(4)−C(4)	160.9(5)	160.6(5)
N(1)−C(1)−N(7)	170.9(5)	170.9(6)
N(2)−C(2)−N(8)	173.0(5)	172.8(6)

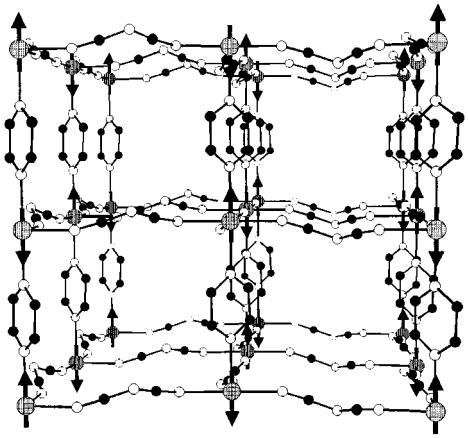

Figure 12. Crystal and magnetic structure of $Mn[N(CN)_2]_2(pyz)$. Arrows denote the spin configuration of the ordered Mn^{2+} moments. Only one of the two interpenetrating lattices is shown. Mn, C, and N atoms are depicted as shaded, filled, and open spheres, respectively.

The spin configuration and magnitude of the Mn^{2+} moments can be determined from the relative intensities of the magnetic Bragg reflections.[30] From the magnetic susceptibility data and electronic structure calculations (see section 3.4), the magnetic easy axis is expected to be parallel to Mn−pyz−Mn chains. Using this information, the spin orientations of the Mn^{2+} moments were fixed parallel to the [100] direction while the nearest-neighboring spins were ordered antiferromagnetically. The spin configuration of the second interpenetrating lattice must also be considered, because it can be the same as or opposite to that of the first lattice.

Three models were employed in solving the magnetic structure. In model I we assumed that the two lattices have opposite spin configurations, and the magnetic structure was refined accordingly. This gave correct peak positions but overcompensated (and reversed) intensity patterns for the (101) and (111) magnetic reflections. In model II we assumed that the two lattices had the same spin orientation, and the magnetic structure was refined allowing only the magnitude of the m_x moment to vary. Model II gave excellent agreement with the neutron powder diffraction data. Hence, the Shubnikov group must also be identical to the crystallographic space group[9] ($P2_1/n$); i.e., the magnetic symmetry of the second interpenetrating lattice carries the same sign of spin ordering as does the first lattice. During the final Rietveld refinement of the 1.35 K neutron data, the lattice parameters, profile parameters, scale factor, and magnetic moment were refined (Figure 9b). Model II could be satisfactorily refined against all data to give a weighted residual fit parameter $R_{wp} = 3.47\%$. From these data, a reduced Mn^{2+} moment of 4.15(6) μ_B was obtained, which is significantly smaller than the expected free ion value of 5 μ_B. This Mn^{2+} moment reduction is not atypical and is ascribed to covalency effects and zero-point spin deviation, phenomena exhibited by several other materials including $Mn[N(CN)_2]_2$,[6b] $MnTe_2$,[31] Cu_2MnSnS_4,[32] and α-MnS.[33]

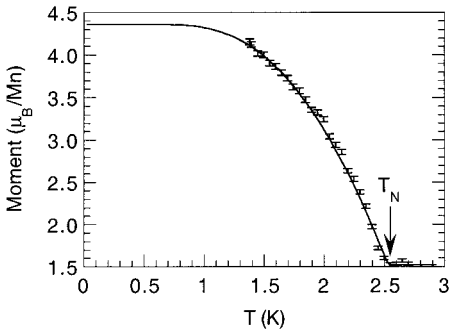

Figure 13. Sublattice magnetization of $Mn[N(CN)_2]_2(pyz)$ taken between 1.35 and 3 K.

To rule out any possibility of a small degree of spin tilting in the *c*-direction, the constraints on the m_z component of the magnetic moment (used in model II) were lifted and allowed to vary in the GSAS refinement. This approach (model III) led to poor results in that no convergence was reached. Therefore, model II afforded the unique solution (Figure 12).

Magnetic Order Parameter. The intensity of the strong (111) reflection was used to measure the temperature variation of the sublattice magnetization of $Mn[N(CN)_2]_2(pyz)$ between 1.35 and 3.0 K (Figure 13). Data were taken from both warming and cooling cycles, which revealed no measurable hysteresis in T_N. Note that, at the lowest temperature measured, a saturated moment is not quite achieved as compared to the fit of the Brillioun magnetization. The T_N is taken as the inflection point at 2.53(2) K, which is in excellent agreement with the value obtained from the other studies. Additionally, fitting of the data to a power law yields $\beta = 0.38$, which is consistent with the value derived for a 3D Heisenberg antiferromagnet.[34]

Field-Dependent Magnetic Structure. With the zero-field magnetic structure in hand, we can make some predictions regarding the spin reorientation which occurs in an applied magnetic field. For $H < 0.43$ T, the spins align parallel to the

(31) Burlet, P.; Ressouche, E.; Malaman, B.; Welter, R.; Sanchez, J. P.; Vulliet, P. *Phys. Rev. B* **1997**, *56*, 14013.
(32) Fries, T.; Shapira, Y.; Palacio, F.; Moron, M. C.; McIntyre, G. J.; Kershaw, R.; Wold, A. McNiff, E. J. *Phys. Rev. B* **1997**, *56*, 5424.
(33) Jacobson, A. J.; Fender, B. E. F. *J. Chem. Phys.* **1970**, *52*, 4563.
(34) Rushbrooke, G. S.; Baker, G. A.; Wood, P. J. In *Phase Transitions and Critical Phenomena*; Domb, C., Green, M. S., Eds.; Academic Press: New York, 1973; Vol. 3.

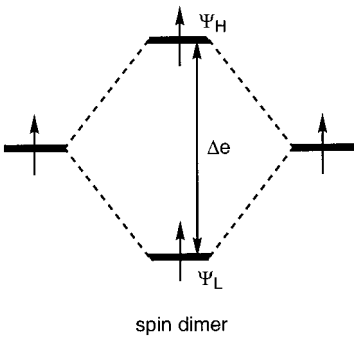

Figure 14. Interaction between adjacent spin−orbitals in a spin dimer leading to the spin−orbital interaction energy Δ*e*.

a-axis. It was shown previously that a spin-flop transition is observed at 0.43 T, which implies that the spins rotate into the *bc*-plane, i.e., perpendicular to the applied magnetic field. Their exact configuration can only be identified by field-dependent neutron diffraction measurements on a single crystal, owing to the complexity of the data analysis afforded by a powder sample. Between the H_{sf} and H_c transition fields, the spins remain highly fluctuating and gradually rotate toward the *a*-direction with increasing *H*. Beyond 2.83 T the spins realign themselves parallel to the *a*-axis, but in a ferromagnetic-like manner.

3.4. Analysis of Spin Exchange Interactions. The spin exchange interactions of a magnetic solid are often described by a spin Hamiltonian made up of nearest-neighbor spin exchange parameters *J*. The *J* parameters can be related to the crystal structure of a magnetic solid by performing appropriate electronic structure calculations for the spin dimers (i.e., structural units containing two adjacent unpaired spins) of the solid. The *J* value of a spin dimer containing two unpaired spins corresponds to the energy difference Δ*E* between the triplet and singlet states of the spin dimer;[35−37] i.e., $J = \Delta E = {}^1E - {}^3E$, where ${}^1E$ and ${}^3E$ are the total energies of the singlet and triplet states, respectively. Thus, the interaction between two spins is ferromagnetic if the triplet state of the spin dimer is more stable than the singlet state, and is antiferromagnetic otherwise. The spin exchange parameter *J* is written as $J = J_F + J_{AF}$, where the ferromagnetic term J_F favors the triplet state (i.e., $J_F > 0$), and the antiferromagnetic term J_{AF} favors the singlet state (i.e., $J_{AF} < 0$). The *J* values for transition metal oxides and fluorides of perovskite-type structures are well reproduced by the Δ*E* values of the corresponding spin dimers determined from first principles electronic structure calculations.[38]

Qualitative trends in the *J* parameters of a magnetic solid are well explained in terms of spin−orbital interaction energies Δ*e* of spin dimers obtained from extended Hückel molecular orbital calculations.[16−19] As shown in Figure 14, the Δ*e* value of a spin dimer is the energy difference between the two singly occupied energy levels (i.e., ψ_H and ψ_L) of the spin dimer.[35] For the antiferromagnetic interaction between two equivalent spins, the J_{AF} term is related to the spin−orbital interaction energy Δ*e* by eq 5 when the singly filled levels of a spin dimer

$$J_{AF} \propto -(\Delta e)^2 \tag{5}$$

are given as linear combinations of orthogonal spin−orbitals at the two spin sites.[35] Alternatively, the J_{AF} term is related to the spin−orbital interaction energy Δ*e* by eq 6 when the singly

$$J_{AF} \propto -S\Delta e \tag{6}$$

filled levels of a spin-dimer are given as linear combinations of nonorthogonal spin−orbitals localized at the two spin sites, and *S* is the overlap integral between the two nonorthogonal spin−orbitals.[36] Due to the relationship $\Delta e \propto S$, eq 6 is qualitatively identical to eq 5.

In Mn[N(CN)$_2$]$_2$(pyz) there are five unpaired electrons at each Mn^{2+} site. When a spin monomer has more than one unpaired spin, consideration of the spin exchange interaction in a spin dimer is modified slightly. Suppose that the spin sites A and B of a spin dimer have n_A and n_B unpaired spins, respectively. The overall spin exchange parameter *J* of the spin dimer is then described by eq 7.[39]

$$J = \sum_{\mu=1}^{n_A}\sum_{\nu=1}^{n_B} \frac{J_{\mu\nu}}{n_A n_B} \tag{7}$$

A spin monomer (i.e., a structural unit containing a single unpaired spin) of Mn[N(CN)$_2$]$_2$(pyz) is given by the {Mn[N(CN)$_2$]$_4$(pyz)$_2$}$^{2-}$ ion, as depicted in Figure 15a by a projection view along the *a*-direction, where pyrazine molecules are presented by dashed lines. There are several different spin dimers to consider. A spin dimer along the *a*-direction is obtained from two spin monomers sharing a pyrazine molecule, while spin monomers along the *b*- and *c*-directions are obtained from two spin monomers sharing an [N(CN)$_2$]$^-$ anion. Therefore, a spin dimer along the *a*-direction is given by the {Mn$_2$[N(CN)$_2$]$_8$(pyz)$_3$}$^{4-}$ ion (Figure 15b), that along the *b*-direction by the {Mn$_2$[N(CN)$_2$]$_7$(pyz)$_4$}$^{3-}$ ion (Figure 15c), and that along the *c*-direction by the {Mn$_2$[N(CN)$_2$]$_7$(pyz)$_4$}$^{3-}$ ion (Figure 15d). To simplify our calculations, we employed the idealized geometries for pyrazine and [N(CN)$_2$]$^-$ as well as the coordinate environment of each Mn^{2+} cation; all pyrazine molecules were made identical with D_{2h} symmetry, and all [N(CN)$_2$]$^-$ anions were made identical with C_{2v} symmetry. The bond lengths and bond angles of these species were fixed at the appropriate average values taken from the slightly different structures found from the crystal structure determination. Each distorted MnN$_6$ octahedron was also idealized by giving a D_{4h} symmetry with the average Mn−N$_{eq}$ and Mn−N$_{ax}$ bond lengths. We also carried out calculations using the real structures to find that use of the ideal and the real structures leads essentially to the same results. Thus, in the following we present only the results obtained from the idealized structures.

Our calculations for the spin monomer show that the d-block energy levels are grouped into the t_{2g} and e_g levels. Given the local coordinate system used for a spin monomer in Figure 15a, the *xy*, *xz*, and *yz* orbitals of Mn belong to the t_{2g} set, while the $x^2 - y^2$ and z^2 orbitals of Mn belong to the e_g set. The pyrazine molecular plane is aligned approximately along the $x + y$ direction so that the linear combination, $xz + yz$, does not interact with the π orbitals of pyrazine, but the linear combination, $xz - yz$, does. Calculations for the spin monomer show that the *xy*, $xz + yz$, and $xz - yz$ levels are nearly the same in energy, the $x^2 - y^2$ level lies 1.3 eV above this t_{2g} set, and the z^2 level lies 0.7 eV above the $x^2 - y^2$ level. With five unpaired spins per Mn^{2+} site, all five d-levels of the spin monomer are each singly occupied. Thus, for each spin dimer of Mn[N(CN)$_2$]$_2$(pyz), eq 6 has 25 terms to consider, i.e., five diagonal

(35) Hay, P. J.; Thibeault, J. C.; Hoffmann, R. *J. Am. Chem. Soc.* **1975**, *97*, 4884.
(36) Kahn, O.; Briat, B. *J. Chem. Soc., Faraday Trans. 2* **1976**, *72*, 268.
(37) Kahn, O. *Struct. Bonding* **1987**, *68*, 89.
(38) Moreira, I. de P. R.; Illas, F.; Calzado, C. J.; Sanz, J. F.; Malrieu, J.-P.; Amor, N. B.; Maynau, D. *Phys. Rev. B* **1999**, *59*, 6593 and references cited therein.
(39) Charlot, M. F.; Kahn, O. *Nouv. J. Chim.* **1980**, *4*, 567.

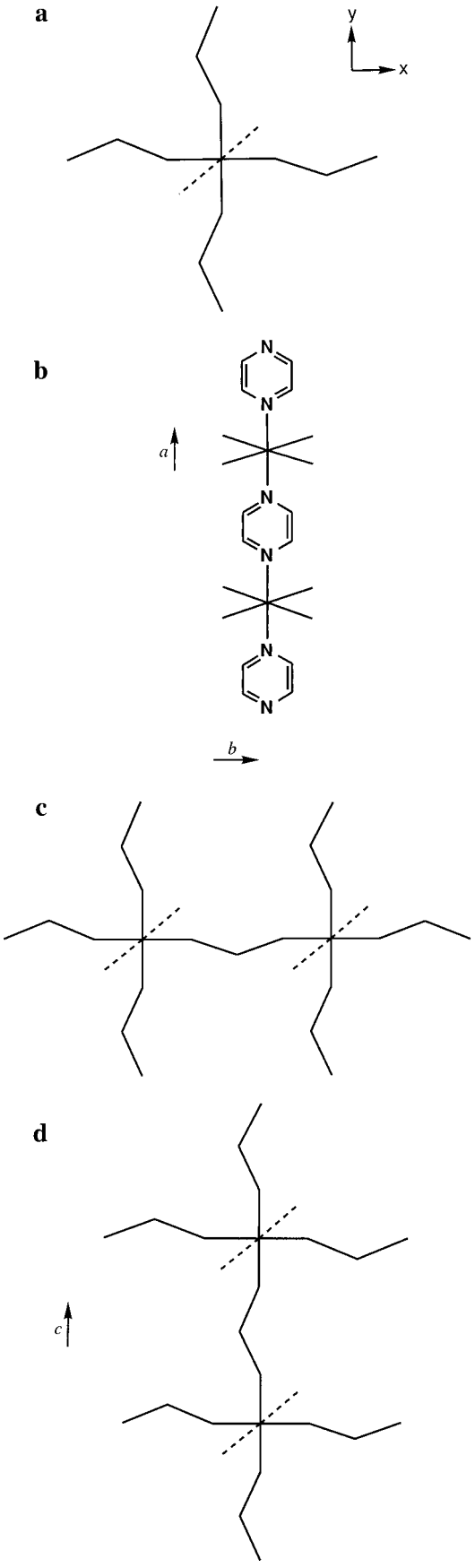

Figure 15. Schematic projection views (along the *a*-direction) of (a) the spin monomer $\{Mn[N(CN)_2]_4(pyz)_2\}^{2-}$, (b) the spin dimer $\{Mn_2[N(CN)_2]_8(pyz)_3\}^{4-}$ along the *a*-direction, (c) the spin dimer $\{Mn_2[N(CN)_2]_7(pyz)_4\}^{3-}$ along the *b*-direction, and (d) the spin dimer $\{Mn_2[N(CN)_2]_7(pyz)_4\}^{3-}$ along the *c*-direction.

Table 3. Spin−Orbital Interaction Energies Δe (in meV) Calculated for the Three Spin Dimers of $Mn[N(CN)_2]_2(pyz)$

d-orbital	along *a*	along *b*	along *c*
z^2	360	21	20
$x^2 - y^2$	4	44	47
xy	0	1	1
$xz + yz$	3	16	16
$xz - yz$	19	16	16

terms ($J_{\mu\mu}$) and 20 off-diagonal terms $J_{\mu\nu}$ ($\mu \neq \nu$). One-electron molecular orbital calculations for a spin dimer provide information about how each d-level of a spin dimer splits as a result of interaction in a spin dimer and hence give the spin−orbital interaction energies associated with the five diagonal terms. From the viewpoint of nonorthogonal spin−orbitals localized at spin centers, the antiferromagnetic contribution J_{AF} to each off-diagonal term $J_{\mu\nu}$ ($\mu \neq \nu$) is expected to be negligible because orbitals of different symmetry have either a zero or a negligible overlap integral. Thus, the main contributions of the off-diagonal $J_{\mu\nu}$ terms will be ferromagnetic. For our qualitative discussion of the antiferromagnetic exchange interactions in $Mn[N(CN)_2]_2(pyz)$, it is sufficient to consider only the spin−orbital interaction energies calculated for the five diagonal $J_{\mu\mu}$ terms (Table 3). This approach was recently shown to be useful for describing the spin exchange interactions of magnetic solids with several spins per spin site.[40]

Figure 16a−d shows the nodal properties of some representative spin dimer ψ_H and ψ_L levels. For simplicity, only the d-orbitals of Mn and the orbitals of the coordinating N atoms of the bridging ligand are shown in each diagram. In all cases, the d-orbitals have opposite signs in the lower-lying level ψ_L and the same sign in the higher-lying level ψ_H. The following are observed from the spin−orbital interaction energies of Table 3: (a) Along the *a*-direction, the spin exchange interactions are dominated by the σ-interaction associated with the z^2 orbitals. (b) Along the *b*- and *c*-directions, the d-orbitals of the e_g set lead to stronger spin exchange interactions than those of the t_{2g} set. Namely, even along the *b*- and *c*-directions, the spin exchange through the σ-interaction is stronger than that through the π-interaction. (c) The σ-interaction is stronger along the *a*-direction than along the *b*- and *c*-directions. This shows that the lone pair orbitals of pyrazine lead to a much more effective superexchange than do the lone pair orbitals of dicyanamide anion.

The spin−orbital interaction energies Δe of Table 3 indicate that the spin exchange interactions of $Mn[N(CN)_2]_2(pyz)$ should be stronger along the *a*-direction than along the *b*- or *c*-direction, in agreement with the finding that the magnetic susceptibility is very well described by a 1D Heisenberg linear chain model. The relative strengths of the spin exchange interactions along the Mn−pyz−Mn and Mn−NCNCN−Mn axes can be estimated by using eq 7. For our rough estimate, we neglect all off-diagonal terms $J_{\mu\nu}$ ($\mu \neq \nu$) as well as the J_F terms of the remaining five diagonal terms $J_{\mu\mu}$. Using eq 5 and the Δe values of Table 3, the spin exchange along the Mn−pyz−Mn axis is estimated to be stronger than that along the Mn−NCNCN−Mn axis by a factor of about 40.

The spin exchange interactions along the *b*- and *c*-axes are similar in magnitude (Table 3). In principle, therefore, the antiferromagnetic interaction through the $[N(CN)_2]^-$ anion bridge could double not only the *c*-axis but also the *b*-axis. It should be noted that, given the lattice parameters $a = 7.3247(2)$,

(40) Whangbo, M.-H.; Koo, H.-J.; Coste, S.; Jobic, S. *J Solid State Chem.*, in press.

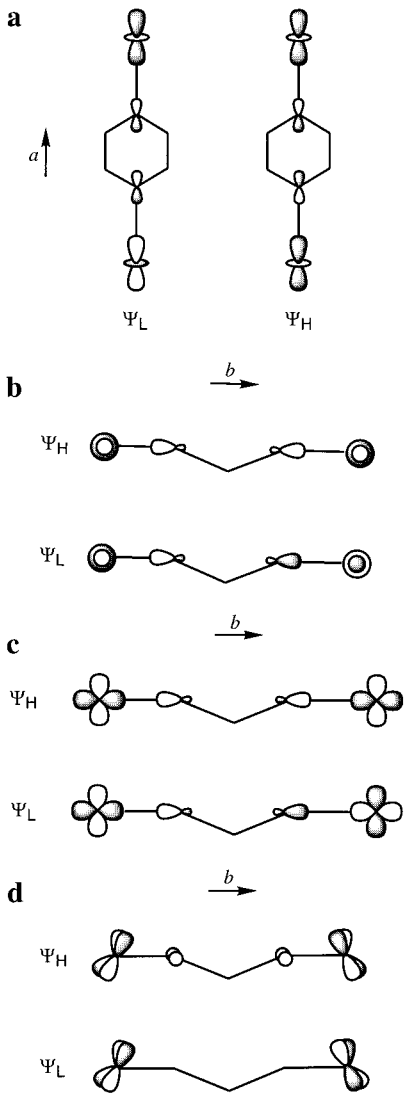

Figure 16. Nodal properties of representative spin dimer orbitals. (a) The z^2 levels of the spin dimer along the *a*-direction. (b) The z^2 levels of the spin dimer along the *b*-direction. (c) The $x^2 - y^2$ levels of the spin dimer along the *b*-direction. (d) The $xz + yz$ levels of the spin dimer along the *b*-direction. Only the d-orbitals of Mn and the orbitals of the coordinating N atoms of the bridging ligand are shown for simplicity. In (b)−(d) the nodal properties are given as projection views in the *xy* plane.

$b = 16.7366(6)$, and $c = 8.7904(3)$ Å of the nonmagnetic lattice, the *b*-axis length is already about twice the *c*-axis length, so the unit cell of the ($^1/_2$, 0, $^1/_2$) superstructure is approximately cubic. Although a weak dipole−dipole exchange interaction could exist between the two interpenetrating lattices, it was not addressed in the calculations but warrants further study.

Bidentate μ-pyz linkages have provided exchange constants, J/k_B, ranging from −0.27 to −7.63 K, for Mn[N(CN)$_2$]$_2$(pyz) and [Cu(pyz)$_2$](ClO$_4$)$_2$,[41] respectively. The magnetic properties of selected metal−pyrazine complexes are presented in Table 4. In general, the spin exchange interaction is stronger for M = Cu than for M = Mn, which is attributed to an improved overlap between the singly occupied $x^2 - y^2$ orbital and the lone pair orbitals of pyrazine.[41] Another important reason leading to this observation is that the Mn^{2+} ion has five spins while the Cu^{2+} ion has one. As shown in Table 3, the z^2 orbital alone should give a strong antiferromagnetic interaction through the pyrazine bridge in Mn[N(CN)$_2$]$_2$(pyz). However, the experimental *J* value of Mn[N(CN)$_2$]$_2$(pyz) shows a weak antiferromagnetic interaction due to competing ferromagnetic interactions arising from the other d-orbitals. For the same reason, the magnitude of the spin exchange parameter is much larger in La_2CuO_4, which has one unpaired spin per Cu^{2+} site, than that in K_2NiF_4, which has two unpaired spins per Ni^{2+} site (−128 meV versus −8.2 meV).[19]

Table 4. Magnetic Properties of Selected Transition Metal−Pyrazine Complexes[a]

compound	magnetic lattice	⟨*g*⟩	J/k_B (K)	refs
Mn(N$_3$)$_2$(pyz)	2D	2.03	−0.24	45
Mn(NCS)$_2$(pyz)$_2$	2D	1.99	−0.29	46
Fe(NCS)$_2$(pyz)$_2$	2D	2.36	−1.47	47
Cu(ClO$_4$)$_2$(pyz)$_2$	2D	2.11	−7.63	41
Cu(CH$_3$SO$_3$)$_2$(pyz)$_2$	2D	2.15	−3.57	48
Cu(NCO)$_2$(mepyz)[b]	2D	2.02	−1.68	49
Mn[N(CN)$_2$]$_2$(pyz)	1D	2.01	−0.27	this work
α-Cu[N(CN)$_2$]$_2$(pyz)	1D	2.14	−3.90	44a
Cu(NO$_3$)$_2$(pyz)	1D	2.12	−5.33	50
Cu(NO$_3$)$_2$(2,6-me$_2$pyz)	1D	2.10	−5.76	50
Cu(NO$_3$)$_2$(2,5-me$_2$pyz)	1D	2.10	−5.04	50
Cu(NO$_3$)$_2$(Cl-pyz)	1D	2.09	−2.02	50
Cu(NO$_3$)$_2$(mepyz)	1D	2.06	−4.46	50
Cu(hfac)$_2$(pyz)[c]	1D	2.24	−0.54	51
Cu(2,3-pyzdc)·HCl[d]	1D	2.26	1.90	52
Cu(pyzc)$_2$[e]	1D	2.12	0.60	53
Cu(pyzc)$_2$(H$_2$O)$_2$	1D	2.15	0.33	53

[a] For magnetic systems with more than one superexchange path, only the M−pyz−M interaction is listed. [b] mepyz = methylpyrazine. [c] hfac = hexafluoroacetylacetonate. [d] 2,3-pyzdc = 2,3-pyrazinedicarboxylate. [e] pyzc = pyrazinecarboxylate.

4. Conclusions

We have shown that Mn[N(CN)$_2$]$_2$(pyz) exhibits a phase transition from a paramagnetic state to an antiferromagnetic state at $T_N = 2.53(2)$ K using magnetic susceptibility, specific heat, and neutron diffraction measurements. The antiferromagnetic structure was found to be collinear with reduced Mn^{2+} moments of 4.15(6) μ_B aligned parallel to the *a*-axis. Results of temperature-dependent magnetic susceptibility and spin dimer analysis reveal a nominal 1D antiferromagnetic chain behavior along the *a*-direction. Isothermal magnetization studies carried out below T_N show a field-induced antiferromagnetic to spin-flop

(41) Darriet, J.; Haddad, M. S.; Duesler, E. N.; Hendrickson, D. N. *Inorg. Chem.* **1979**, *18*, 2679.
(42) For example: McGregor, K. T.; Soos, Z. G. *J. Chem. Phys.* **1976**, *64*, 2506.
(43) For example: Lynn, J. W.; Clinton, T. W.; Li, W.-H.; Erwin, R. W.; Liu, J. Z.; Vandervoort, J.; Shelton, R. N. *Phys. Rev. Lett.* **1989**, *63*, 2374.
(44) (a) Manson, J. L., to be published. (b) Jensen, P.; Batten, S. R.; Fallon, G. D.; Hockless, D. C. R.; Moubaraki, B.; Murray, K. S.; Robson, R. *J. Solid State Chem.* **1999**, *145*, 387.
(45) Manson, J. L.; Arif, A. M.; Miller, J. S. *Chem. Commun.* **1999**, 1479.
(46) Lloret, F.; Julve, M.; Cano, J.; De Munno, G. *Mol. Cryst. Liq. Cryst.* **1999**, *334*, 569.
(47) Real, J. A.; De Munno, G.; Munoz, M. C.; Julve, M. *Inorg. Chem.* **1991**, *30*, 2701.
(48) Haynes, J. S.; Rettig, S. J.; Sams, J. R.; Thompson, R. C.; Trotter, J. *Can. J. Chem.* **1987**, *65*, 420.
(49) Otieno, T.; Rettig, S. J.; Thompson, R. C.; Trotter, J. *Inorg. Chem.* **1993**, *32*, 4384.
(50) Richardson, H. W.; Hatfield, W. E. *J. Am. Chem. Soc.* **1976**, *98*, 835.
(51) Richardson, H. W.; Wasson, J. R.; Hatfield, W. E. *Inorg. Chem.* **1977**, *16*, 484.
(52) (a) O'Connor, C. J.; Klein, C. L.; Majeste, R. J.; Trefonas, L. M. *Inorg. Chem.* **1982**, *21*, 64. (b) Burriel, R.; O'Connor, C. J.; Carlin, R. L. *Inorg. Chem.* **1985**, *24*, 3706.
(53) Klein, C. L.; Majeste, R. J.; Trefonas, L. M.; O'Connor, C. J. *Inorg. Chem.* **1982**, *21*, 1891.

transition at 0.43 T and a spin-flop to paramagnetic transition at 2.83 T. A λ-shaped anomaly in the specific heat data confirmed the presence of the magnetic phase transition. A μ-nitrile-bonded dicyanamide is a largely insufficient exchange mediator in coordination solids of this type and promotes low magnetic ordering temperatures. Coordination of both the amide-N atom and one of the nitrile-N atoms may provide a stronger magnetic interaction through a three-atom pathway, but this bonding mode has not yet been observed experimentally. Moreover, the possibility of dipolar exchange coupling between the two interpenetrating lattices cannot be ruled out and warrants further investigation. Work is continuing in an effort to determine the 1D spin correlations using EPR[42] and neutron diffraction.[43] Other members in the $M[N(CN)_2]_2(pyz)$ {M = Cr, Fe, Co, Ni, Cu[44]} family are also being examined.

Acknowledgment. Work performed at the University of Utah, North Carolina State University, and Argonne National Laboratory was supported by the Office of Basic Energy Sciences, Division of Materials Science, U.S. Department of Energy, under Grants DE-FG03-93ER45504, DE-FG05-86ER45259, and W-31-109-ENG-38, respectively. J.L.M. gratefully acknowledges P. Rivett (Oxford Research Instruments) for the VSM measurements and K. Awaga and C. R. Kmety for helpful discussions. Identification of commercial equipment in the text is not intended to imply any recommendation or endorsement by the National Institute of Standards and Technology.

JA0024791